Journal of Power Sources 473 (2020) 228579

Contents lists available at ScienceDirect

Journal of Power Sources

journal homepage: www.elsevier.com/locate/jpowsour

Enabling high areal capacity for Co-free high voltage spinel materials in next-generation Li-ion batteries

Weikang Li [a], Yoon-Gyo Cho [a], Weiliang Yao [b], Yixuan Li [a], Ashley Cronk [b], Ryosuke Shimizu [a], Marshall A. Schroeder [c], Yanbao Fu [d], Feng Zou [e], Vince Battaglia [d], Arumugam Manthiram [e], Minghao Zhang [a,**], Ying Shirley Meng [a,b,*]

[a] Department of NanoEngineering, University of California San Diego, La Jolla, CA, 92093, USA
[b] Materials Science and Engineering, University of California San Diego, La Jolla, CA, 92093, USA
[c] Energy Storage Branch, Sensors and Electron Devices Directorate, U.S. Army Research Laboratory, Adelphi, MD, 20783, USA
[d] Energy Storage and Distributed Resources Division, Lawrence Berkeley National Laboratory, Berkeley, CA, 94720, USA
[e] Materials Science and Engineering Program & Texas Materials Institute, University of Texas at Austin, Austin, TX, 78712, USA

HIGHLIGHTS

- Inactive components in LNMO cathode have significant impact on cycling stability.
- 3 mAh/cm^2 LNMO electrode paired with graphite shows superior cycle stability.
- Degradation is triggered by graphite failure through cross-talk with LNMO cathode.

ARTICLE INFO

Keywords:
Cobalt-free cathode
High voltage spinel
$LiNi_{0.5}Mn_{1.5}O_4$
Thick electrode
Full cell cycling

ABSTRACT

The rapidly growing technological demand for lithium-ion batteries has prompted the development of novel cathode materials with high energy density, low cost, and improved safety. High voltage spinel, $LiNi_{0.5}Mn_{1.5}O_4$ (LNMO), is one of the most promising candidates yet to be commercialized. The two primary obstacles for this material are the inferior electronic conductivity and fast capacity degradation in full cells due to the high operating voltage. By systematically addressing these limitations, we successfully develop a thick LNMO electrode with areal capacity loadings up to 3 mAh·cm^{-2}. The optimized thick electrode is paired with a commercial graphite anode at both the coin cell and pouch cell level, achieving a full cell capacity retention as high as 72% and 78%, respectively, after 300 cycles. We attribute this superior cycling stability to careful optimizations of cell components and testing conditions, with a specific focus improving electronic conductivity and high voltage compatibility. These results suggest precise control of materials quality, electrode architecture and electrolyte optimization can soon support the development of a cobalt-free battery system based on a thick LNMO cathode (>4 mAh·cm^2), which will eventually meet the needs of next-generation Li-ion batteries with reduced cost, improved safety, and assured sustainability.

1. Introduction

The rapid expansion of portable electronics, electric vehicles, and household energy storage devices have injected a surge of power into the development of lithium-ion batteries (LIBs). It is commonly acknowledged that lithium-ion batteries will, as always, play an essential role in energy storage. To meet the ever-increasing demands, the main performance metrics, including energy density, cycle life, safety, cost, etc. of LIBs require significant improvement. As an essential component of LIBs, the cathode material, to a large extent, determines the electrochemical performance of the whole battery system. Classical layered lithium cobalt oxide ($LiCoO_2$) is currently used in 3C products due to its high volumetric energy density [1], which meets the micromation demand for portable products. As for electric vehicles, cathode materials

* Corresponding author. Department of NanoEngineering, University of California San Diego, La Jolla, CA, 92093, USA.
** Corresponding author.
E-mail addresses: miz016@eng.ucsd.edu (M. Zhang), shirleymeng@ucsd.edu (Y.S. Meng).

https://doi.org/10.1016/j.jpowsour.2020.228579
Received 24 April 2020; Received in revised form 18 June 2020; Accepted 27 June 2020

such as $LiMn_2O_4$, $LiFePO_4$, and Ni-rich NCA/NCM are mainly adopted under the consideration of cost and energy density. The capacities of olivine $LiFePO_4$ and spinel $LiMn_2O_4$ are limited in satisfying the demands of high energy density for electric vehicle applications [2,3]. The development of Ni-rich layered oxide materials with high energy density has flourished in recent years, but their cost has been affected by both cobalt and nickel. And so far, the single-cell price based on this kind of material is still beyond expectation [4]. These difficulties have generated considerable worldwide efforts to seek alternative cathode materials with high energy density and assured sustainability.

Advancing cathode materials with both high energy density and low cost have always been the main objective of battery material research. Developing cobalt-free cathode materials is one of the significant concepts to lower down the price of current LIBs [5]. Dahn et al. doped light elements such as Mg and Al to replace Co in Ni-rich materials [6,7], they made progress on entirely replacing cobalt with the acceptable loss of cycle retention, but still needed further optimization to lower down the cost. Ceder et al. applied a broader range of transition metal elements and designed lithium-rich disordered materials [8–10], however low electronic conductivity is the principal disadvantage of these disordered rock-salt materials, leading to the impossibility of immediate commercialization. Cobalt-free type of lithium-rich manganese-based materials are also promising, but severe voltage decay and low tap density hindered these materials from being commercialized for years [11,12].

It should be noted, the cost and sustainability of lithium-ion batteries

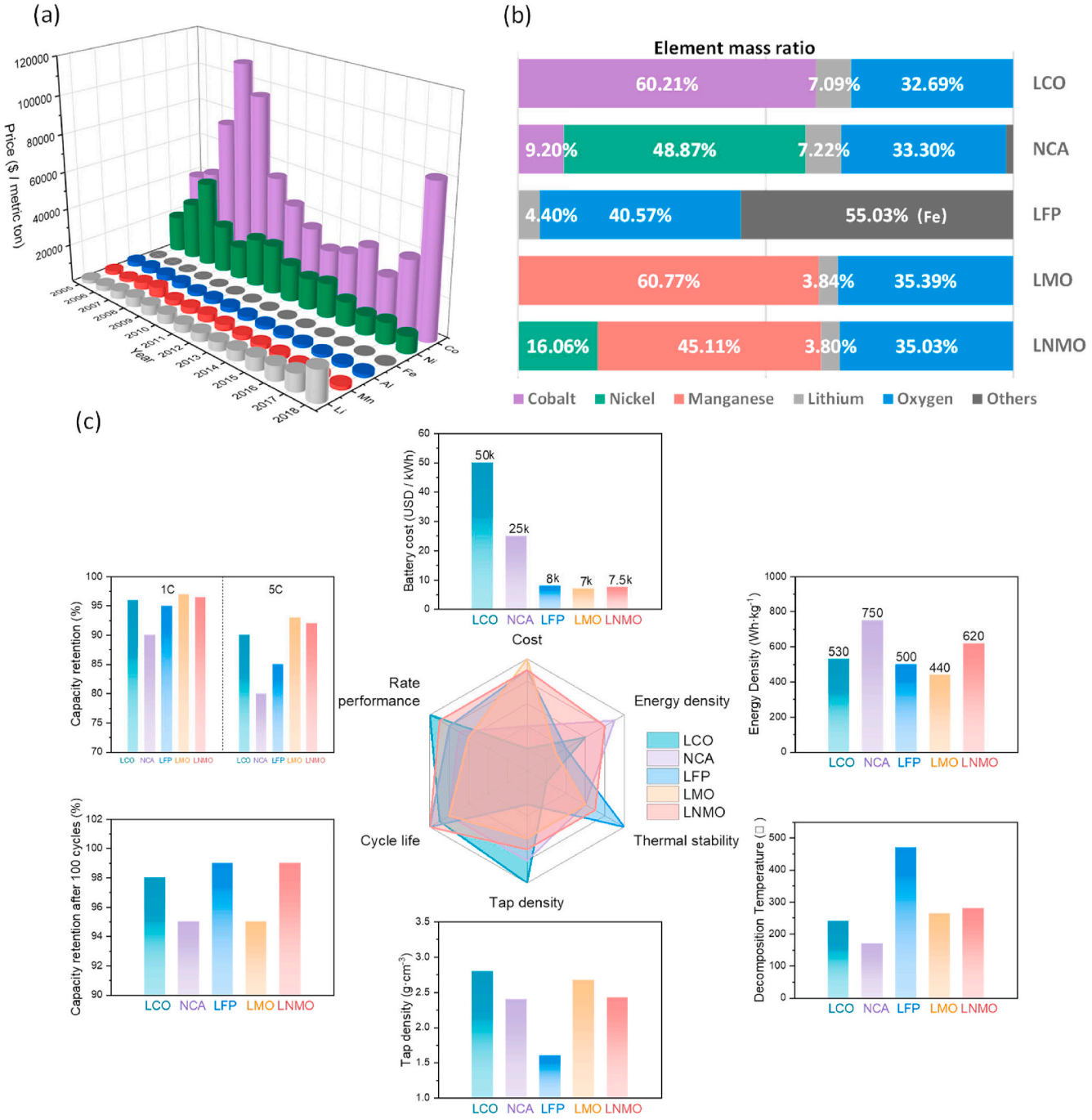

Fig. 1. (a) Annual price of Li, Mn, Al, Fe, Ni and Co elements (source: metalary.com); (b) element mass ratios in five common cathode materials; (c) benchmark radar map for five widely used cathode materials (detailed data sources are listed in supplementary information Table S1).

are not only limited by the production of Co and Ni but also potentially limited by the lithium element itself. Fig. 1(a) summarizes the trend of different elements price changes over the past several years. The price of Co fluctuates significantly, with the inconspicuous fall of Ni price and continues growing of Li price. It is expected that with the large-scale popularization of electric vehicles and energy storage, the price and consumption rate of lithium resources will be even higher. Developing cathode material with less lithium and cost-effective elements such as Mn/Fe/Al is thus quite imperative.

The high-voltage spinel LNMO ($LiNi_{0.5}Mn_{1.5}O_4$) has attracted wide attention since it can deliver a high mass-specific energy density and a high operating voltage (4.7 V) [13,14]. More importantly, it does not contain expensive cobalt or an excessive amount of lithium, which makes LNMO cost-effective and suitable for applications in the field of power batteries and large-scale energy storage [15–17]. Fig. 1(b) illustrates the elemental mass ratios in different types of cathode materials including $LiCoO_2$ (LCO)/$LiNi_{0.8}Co_{0.15}Al_{0.05}O_2$ (NCA) / $LiFePO_4$ (LFP) / $LiMn_2O_4$ (LMO) / $LiNi_{0.5}Mn_{1.5}O_4$ (LNMO) that have been applied on a large scale. The high-voltage LNMO material has just 3.84 wt% of Li content but can deliver the second highest specific energy density at cathode level among all the widely used material. Detailed performance metrics comparisons based on the material level (half cell) are shown in Fig. 1(c), including cost, energy density, thermal stability, tap density, cycle life, and rate performance. The LNMO material exhibits the most balanced capability compared to its competitors and can adapt to the different demands of EV batteries, including high energy density and rate performance, low cost, and safety. In addition, the high average operating voltage can effectively reduce the number of single cells for the pack system, thus further improving the volumetric energy density.

Despite its high energy density and low cost, the LNMO material must overcome several challenges to reach commercialization [16,18]. The first challenge is the voltage stability of the battery system. The high operating voltage may not be harmful to the LNMO cathode itself but causes severe decomposition of carbonate-based electrolytes and other cell components. These by-products after decomposition cause fast decay of the whole battery system and even raise safety issues [19]. The second major challenge is the inferior electronic conductivity (see Table S2), which impedes commercial viability but may not impact lab-scale experiments since the electrodes are typically (less than 50 μm) [20]. When the loading of the electrode reaches the industrial level (up to several hundreds of micrometers [21]), the electrochemical reaction kinetics of the electrodes will be much worse if all other electrode performance metrics are kept constant (e.g., electrode density, porosity, and tortuosity).

Herein, we benchmark for the first time the electrochemical performance of a thick LNMO electrode with an areal capacity loading of ~3 $mAh{\cdot}cm^{-2}$ in both coin cells and pouch cells (comparisons on published paper with different areal capacity loading of LNMO are listed in Table 1). Our results show that every single component in the cell can have a significant influence on long-term cycling stability. The capacity decay in both the coin cell and the pouch cell can be ascribed to the complex cross-talk between the positive and negative electrode. Through delicate engineering control, the LNMO material in the thick electrode has excellent potential and is expected to make significant progress, especially coupled with a novel electrolyte system, to move towards industrialization.

Table 1
LNMO-Graphite full cell literature review.

Cycle	Retention (%)	Cathode loading ($mg{\cdot}cm^{-2}$)	Rate (1C = 147 mA g^{-1})	Cell type	Literature
300	**78**	**22**	**0.333**	**Pouch cell**	**This work**
300	**72**	**22**	**0.333**	**Coin cell**	**This work**
100	70	21.3	1	coin cell	[22]
200	60	19.7	1	coin cell	[23]
200	79	15.9	0.2	coin cell	[24]
820	80	15	1	coin cell	[25]
445	82	15	0.5	coin cell	[26]
1000	69	14.7	0.5	coin cell	[15]
100	86.8	14.7	0.333	coin cell	[27]
100	75	12.5	0.333	Swagelok type	[28]
300	90	11	1	/	[29]
400	66	10.96	2	coin cell	[30]
150	76.9	6.5	0.5	coin cell	[31]
200	73	6	0.2	Swagelok-type	[32]
100	75	6	0.5	coin cell	[33]
100	92.5	5.3	0.333	coin cell	[34]
100	81	3.97	0.5	coin cell	[35]

2. Experimental procedures

2.1. Materials preparation and characterizations

All the materials in this paper are from vendors (listed in Table S3); three kinds of LNMO materials as NM-LNMO, NE-LNMO, and HT-LNMO were applied. The details of these three LNMO materials are listed in the supplementary information, including the refined X-ray powder diffraction (XRD) results (Figure S1 and Table S4), scanning electron microscopy (SEM) images (Figure S2), and inductively coupled plasma mass spectrometry (ICP-MS) results (Table S5). For the XRD test, Rigaku SmartLab® diffractometer was applied on the pristine LNMO powders, the scan range was 15°–80° with the step mode, the step size and duration time were set to be 0.02° and 2 s, respectively. The testing voltage and current were 40 kV and 44 mA, respectively, the General Structure Analysis System II (GSAS-II) was employed for the Rietveld refinement [36]. The powders of pristine electrodes and electrodes after 30 cycles with different conductive agents or binders were collected in the glove box and sealed in glass capillaries for the X-ray diffraction test. The transfer process was air-tight to avoid any influence from moisture or oxygen. The tests were carried out on a Bruker X8-ApexII CCD diffractometer equipped with Mo Ka radiation at 50 kV and 50 mA. For the SEM test, FEI Apreo® was applied with 5 kV as the accelerating voltage and 0.1 nA as the beam current. The chemical compositions of different LNMO materials were confirmed by ICP-MS (iCAP RQ, Thermo Fisher Scientific), 40 mg of LNMO powder was dissolved in concentrated HCl (3 mL) overnight and diluted with DI water (22 mL). The ICP sample solution was prepared by mixing the LNMO-dissolved solution (25 μL) with 25 mL of 0.5% HCl + 0.5% HNO_3 solution.

Three different kinds of conductive agents (abbreviated as CA-1, CA-2, and CA-3), three different kinds of binder (abbreviated as B-1, B-2, and B-3), and two different kinds of coin cell cases (abbreviated as SS304 and Al-clad) were also compared with one of the LNMO materials for the high voltage compatibility, details of the best sample were listed in the Table S6, S7, and S8. All the raw materials were thoroughly dried at 120 °C overnight before any application with no other pre-treatment.

2.2. Electrochemical performance measurements

The electrode was fabricated by doctor blade method, firstly, the selected binder and N-Methyl-2-Pyrrolidone (NMP, ≥ 99%, Sigma-Aldrich) were mixed through the mixer (ARE-310, Thinky Corporation, Japan) in a plastic jar with 6 ZrO_2 beads for 10 min, the typical amount of binder and NMP was 0.25 g and 9 mL, respectively. Then the beads were taken out, and the 4.5 g LNMO powder and the selected 0.25 g conductive agent were added into the solution (for the active material: conductive agent: binder = 90:5:5, the mass amount with different ratio would be adjusted accordingly), then mixed for another 1 h. The slurry was applied on the aluminum foil (thickness ≈ 18 μm) and cast by a blade with selected gap thickness, then dried at 60 °C under vacuum overnight to slowly remove the NMP followed by 120 °C for 1 h before

taking out. Details of the casting, including the thickness control, can be found in Figure S3 and Table S9. To control the porosity of the cathode, a hydraulic press was used. The relationship between the porosity of electrode and hydraulic loading is listed in Table S10, attached to the calculation method. The cross-section images of both thick cathode and anode are illustrated in Figure S4, with the related information in Table S11. The conductivities of electrodes were measured by a four-point collinear probe (Keithley 2400), a 2.54 cm × 2.54 cm piece was applied, the related schematic plot can be found there-in-after. The EIS test was done on SP-150 (Biologic, USA) using the coin half cells, and the frequency range is 1 MHz to 1 Hz.

More details of the coin cell and pouch cell setups can be found in Table S12 (half cell-coin cell type), Table S13 (full cell-coin cell type), and Figure S5/Table S14 (pouch cell design with the attached pressure control fixture). All the coin cells were assembled in the glove box with moisture control ($H_2O \leq 0.5$ ppm). The pouch cells were first assembled in the atmosphere without electrolyte, and then the dry pouch was dried at 80 °C overnight under vacuum before the electrolyte injection. After electrolyte injection, the pouch cell was vacuum sealed in the moisture-controlled glove box. The electrochemical performances of all the electrodes were tested at room temperature either by Neware Battery Test System (Neware Technology Ltd., China) or Arbin BT2000 instruments (Arbin instrument, USA), and the electrolyte for all the electrochemical test was Gen2 (EC: EMC = 3: 7 wt% with 1 mol L^{-1} $LiPF_6$) from Gotion company (USA).

To reassemble the cycled electrode into a half cell, the hydraulic crimper with disassembling die (MSK-110, MTI, Corporation, USA) was used to disassemble the cycled cell. Then the electrode was directly assembled into a half cell. For the pouch cell disassembly, the pouch bag was cut, and the electrode piece was collected. A punch tool was applied to get the proper size of the disk electrode and then reassembled into a half cell. All these procedures were conducted in the glovebox. Those cycled electrodes were directly reassembled without further treatment so that the voltage status of the electrode and the substances on the

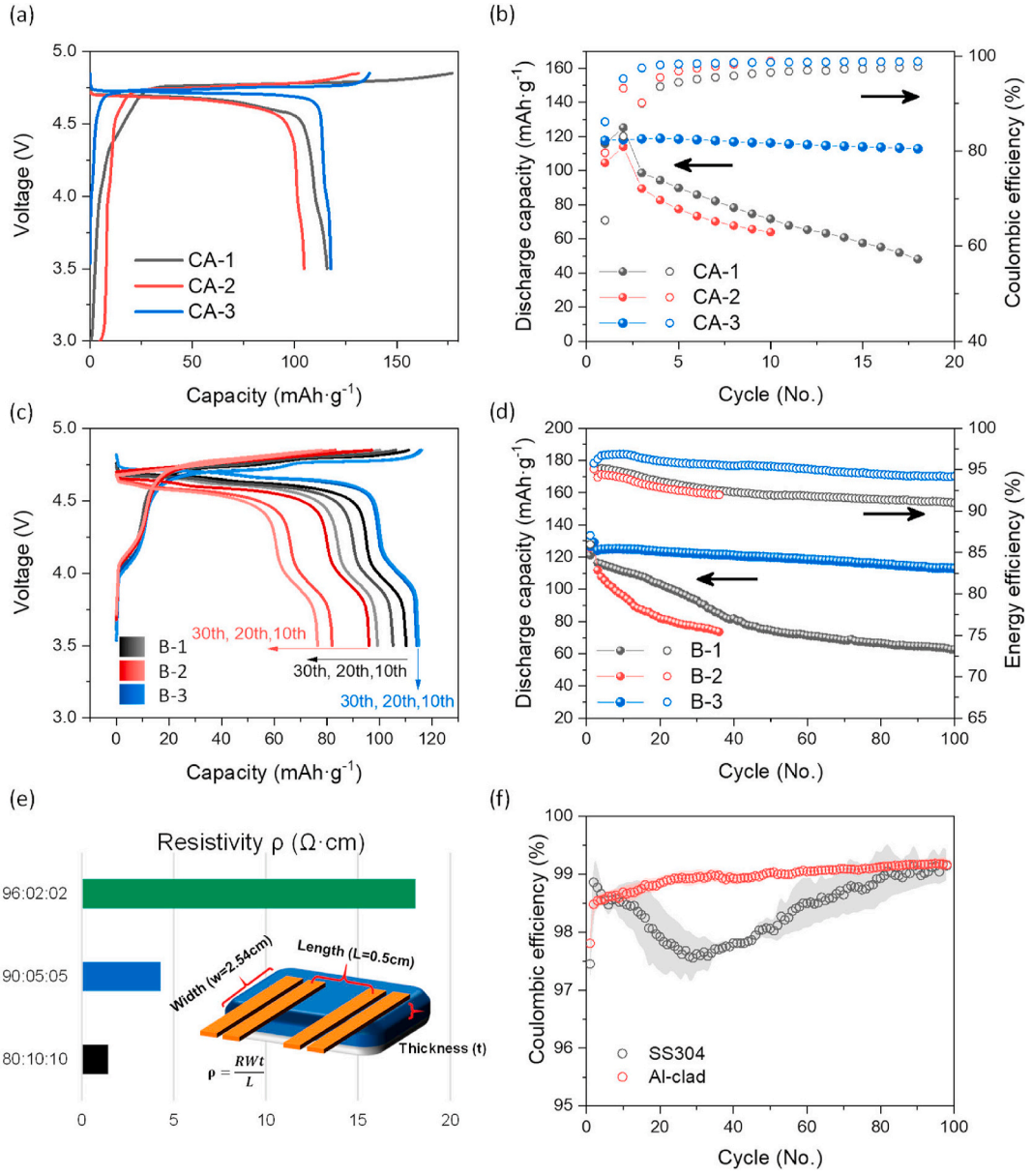

Fig. 2. (a) Initial charge-discharge voltage profiles and (b) cycling performance of electrodes with the different conductive agent in the half cell; (c) charge-discharge voltage profiles of different cycles and (d) cycling performances from electrodes with different binders; (e) four-point probe test for resistivities of electrodes with different composition ratios; (f) Coulombic efficiencies from cells using different coin cell cases.

electrode can be kept all the same before and after the reassembly. The reassembled coin cell followed the same testing protocol as normal half cells.

3. Results and discussion

The cell components were systematically evaluated to achieve stable cycling performance with the high voltage cathode material. First, the compatibility of the conductive agent was evaluated using a thin LNMO electrode (~0.8 mAh·cm^{-2}) with a weight ratio of 8: 1: 1 (active material: binder: conductive agent). Fig. 2(a) shows the charge and discharge curve of the initial cycles using NM-LNMO material mixed with different conductive agents. The electrode with CA-1 has an extended anomalous platform after the Ni redox region (around 4.7 V vs. Li/Li$^+$ corresponding to the Ni^{2+}/Ni^{3+} and Ni^{3+}/Ni^{4+} transitions) during the initial charging process [37]. This indicates the incompatibility of this conductive agent with high voltage exposure, directly leading to an excess side reaction and a low initial Coulombic efficiency. In contrast, electrodes with CA-2 and CA-3 have no excess charging capacity, and CA-3 delivers a higher reversible capacity. As shown in Fig. 2 (b), the LNMO electrode with CA-3 exhibits the best cycling performance among the three different conductive agents. The Coulombic efficiency on each cycle of the CA-3 electrode is also higher than the other two. It is worth noting that among all three conductive agents, CA-3 exhibits the smallest specific surface area, which can help to suppress side reactions during the high-voltage region [38]. Therefore, CA-3 was chosen for the rest of the study due to the best compatibility with LNMO materials.

Similarly, the binder was screened with NE-LNMO material, which has a higher capacity from Mn redox (around 4 V, which corresponds to the Mn^{3+}/Mn^{4+} transition) than the NM-LNMO. Rietveld refined of XRD patterns show that NE-LNMO material can be well indexed to the disordered phase while the NM-LNMO sample matches the $P4_332$ space group. A Higher Mn/Ni ratio is also found for the NE-LNMO sample based on the ICP results, resulting in Mn^{3+} presence in the pristine material. Detail sample information can be found in Figure S1/Table S4 and Table S5. As shown in Fig. 2(c) and (d), the B-1 and B-2 binder performed poorly under high voltage exposure for long cycles. The related dQ/dV plot is illustrated in Figure S6, which clearly shows that the redox peak shifts to the right during the charging process and to the left during the discharge process. This indicates the increase of impedance as cycling progressed, as also confirmed by the continuing lower energy efficiencies of the B-1/B-2 than that of B-3 in Fig. 2(d). It can be inferred that the gradual failure of the binder is due to its incompatibility with high voltage operation, resulting in the contact loss at both the electrode/current collector interface and between the LNMO (carbon) particles [39]. The physical performances of different binders, such as viscosity (see Table S6 for more details), have a significant impact on the adhesion of different components inside the electrode [40]. This impact is undoubtedly amplified under the condition of high voltage operation so that only the electrode with B-3 remains stable during extended cycles. The capacity retention of the B-3 electrode is around 90% after 100 cycles, showing the remarkable high-voltage compatibility.

To further prove the importance of choosing the proper binder and conductive agent, the post-mortem XRD and SEM tests were conducted on all the pristine and cycled electrodes with different conductive agents/binders. The results are shown in Figure S6 and Figure S7. For the conductive agent, the pristine morphologies of the electrodes are different to each other as shown in Figure S6(a), (c) and (e). The porosity of the CA-1 electrode is larger than the other two due to the highest surface area and the smallest volume of CA-1 sample. After 30 cycles at C/3, the surfaces of the electrodes were all covered with side reaction products. The porosity of CA-1 decreased while the by-products of CA-2 covered all the electrode so that the LNMO powder could not be seen from the SEM image. The morphology change of CA-3 electrode after cycling is not as evident as the other two, which indicate the stability of the CA-3 conductive agent. XRD results in Figure S6(g) further confirm this finding. Although the diffraction peaks from LNMO itself have no obvious change, the cycled CA-1 electrode shows more crystalline by-products than CA-2 and CA-3 electrode [41]. As for the different binders, the SEM images of the pristine electrodes in Figure S7 (a), (c) and (e) show similar morphology. While after cycling, B-2 electrode surface has much more side product coverage than the other two, which owns the worst cycle stability. The difference between B-1 and B-3 is negligible. The XRD results on B-1, B-2, and B-3 electrode in Figure S7(g) show no obvious change before and after cycling, which indicating the coverage on all those electrodes after cycling are amorphous.

To coat the thick electrode, the ratio of binder and conductive agent should be limited since both have low density and high surface area. Their low density will not only decrease the overall thick electrode density but also results in excess side reactions under high voltage cycling. However, if the ratio of the binder and the conductive agent is too small, the conductive network may unevenly distribute in the thick electrode, resulting in poor rate performance. Here, we adopted three different ratios, aiming to increase the proportion of active material while keeping acceptable electrode conductivity because of LNMO materials low intrinsic electronic conductivity. The conductivity tests of the electrode with different ratios were performed by the four-probe method. The schematic is shown in Fig. 2(e). It can be found that the resistivity will significantly increase for the electrode having more than 95% active material by weight ratio. This is also consistent with the electrochemical impedance spectroscopy test, as the Nyquist plots of half cells with different ratios shown in Figure S9, attached with the equivalent circuit model and the stimulated R_{ct} value. Here the R_{ct} corresponds to the charge-transfer resistance, which is related to the electronic conductivity of the electrode [11]. Therefore, we adopted 90: 5: 5 as the ratio for the subsequent research. Besides, it was reported that the coin cell cases made of SS304 stainless steel are not robust to withstand voltages above 4.5 V [41]. The side reactions between coin cell cases and electrolyte may affect the long-term cycling performance, which can be reflected by Coulombic efficiency. Two different kinds of coin cell cases are compared here, one is the SS304 stainless steel, and the other is the alumina-clad stainless-steel case. The Coulombic efficiency for the Al-clad case reaches 99% in the early stage and is much higher than that of the ordinary SS304 stainless steel case. The efficiency of the ordinary case decreases at the beginning of the cycle and achieve a similar Coulombic efficiency as the Al-clad steel case only after 100 cycles. It should be noted the components optimization process including binder, conductive, coin cell cases, etc. for the LNMO material can also be applicable for other electrode material working at high voltage, including layered/disordered Li-excess material (typically up to 4.8 V) to achieve better cycling stability [42–45].

After optimizing all the components, the LNMO electrodes with different thicknesses were tested in half cells. It can be found from Fig. 3 (a) that when the electrode is thin (areal capacity loading of 0.5 or 0.8 mAh·cm^{-2}), the cycling of the LNMO material is stable, showing no noticeable decay within 30 cycles. When the areal capacity loading increases to 2.5 or even 3 mAh·cm^{-2} (corresponding to ~18 mg cm^{-2} and ~22 mg cm^{-2}, respectively), the cycle performance of the electrode becomes much worse. After 30 cycles at the C/3 rate, the capacities of both thick electrodes reduce to less than 30% of the initial value. To identify the cause, the cycling current was reduced to C/10 for a 3 mAh·cm^{-2} LNMO electrode during the charge and discharge process. As shown in Fig. 3(b), the capacity shows a negligible fluctuation for more than 30 cycles and then quickly drops. However, the decayed half cell was disassembled, and the cycled thick LNMO electrode was collected and then reassembled into the half cell. The capacity can be fully recovered for several subsequent cycles. Therefore, it can be concluded that the degradation of the thick LNMO electrode is more due to the decay of lithium metal and the decomposition of the electrolyte instead of the cathode itself [46]. This common phenomenon implies the half

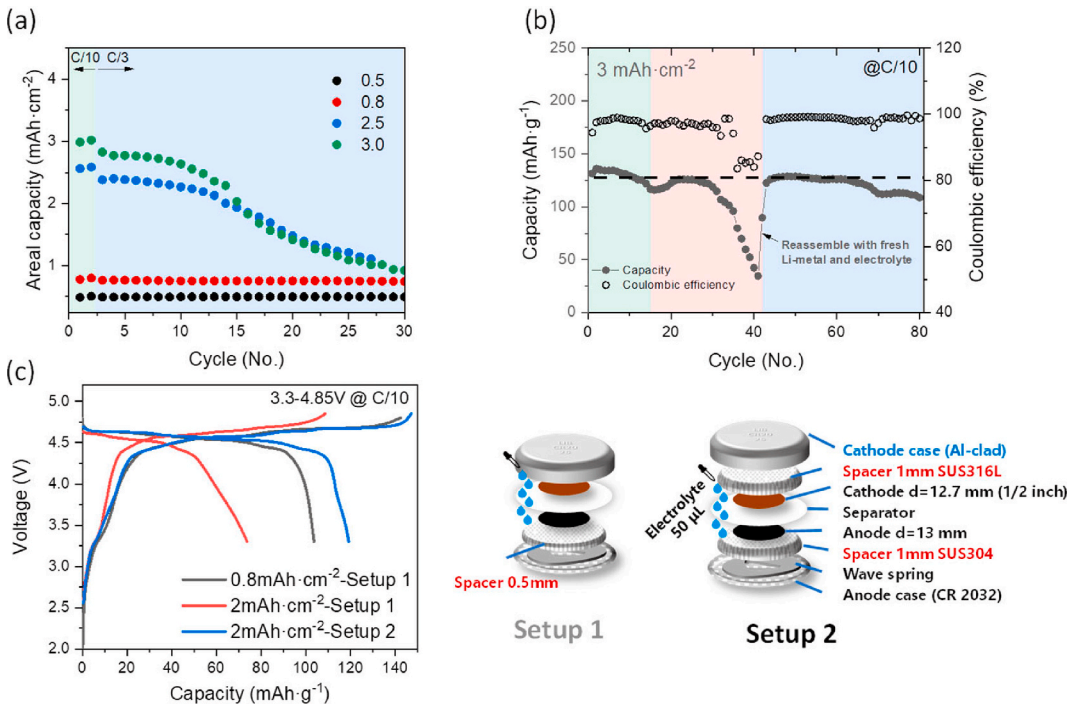

Fig. 3. (a) Half cell cycling performance of electrodes with different areal capacity loading; (b) the half cell cycling performance of a 3 mAh·cm^{-2} thick LNMO electrode and the reassembly test; (c) initial charge-discharge voltage profiles of 2 mAh·cm^{-2} full cells with different coin cell setups and the schematic drawings.

cell limitations for evaluating long-term cycling stability of thick electrode that relevant to the industrial level applications.

The full cell test was then conducted, starting from the thin electrode (0.8 mAh·cm^{-2}). The typical full cell setup was applied at the beginning, labeled as setup-1 in Fig. 3(c). The initial charge and discharge profiles show representative Ni redox plateau at around 4.6 V, and the initial capacity reaches 142 mAh·g^{-1}. When applying the same coin cell setup to thicker LNMO (2.2 mAh·cm^{-2}) paired with 2.4 mAh·cm^{-2} graphite, the initial cycling profiles show higher impedance and much lower capacity. The larger impedance and overpotential can be caused by the insufficient contact between the cathode and anode during cycling. During the high voltage charging process, the decomposition of the electrolyte solvent molecules leads to gas formations such as CO_2 and C_2H_4 [47]. These gas species can act as the ions/electrons isolation islands, thus increasing the cell internal impedance. This can well explain the significant capacity loss mainly comes from the high-voltage region for the thicker electrode. To tackle this problem, one more 1 mm spacer was placed at the cathode side, and the spacer thickness on the anode side was also increased from 0.5 mm to 1 mm, as setup-2 shown in Fig. 3(c). The LNMO-graphite full cell using the optimized coin cell setup resolves the impedance issue and delivers the initial charge capacity of 147 mAh·g^{-1}, which is close to the theoretical capacity from LNMO. The corresponding discharge capacity and Coulombic efficiency are as high as 119.2 mAh·g^{-1} and 81%, respectively. It is proposed that the increased stacking pressure induced by thicker spacers in the cell can effectively squeeze the formed gas out of the center area where the electrochemical reaction occurs. This will help maintain good electrode contact during cycling to reduce cell impedance and improve energy efficiency. As a result, the thicker electrode with the optimized cell setup delivers even better initial cycling performance than the thinner electrode with the typical setup. Note that the total thickness of the coin cell components is restricted by the selected type. More importantly, the stacking pressure of the coin cell after crimping can be hardly monitored so that large-format pouch cell is recommended for this system to obtain more consistent testing results.

To further verify the gassing and pressure effect on the LNMO-graphite full cell system, a 2 mAh·cm^{-2} single layer pouch cell with customized size was made. The initial three cycles as the formation process were performed inside a unique pressure control fixture. More details of the pouch cell and the fixtures can be found in Figure S5 and Table S14. A stacking pressure of 1100 kPa on the electrode area was accurately applied during the initial three cycles as the formation process. Then the pressure control fixture was taken away, and the pouch cell was cycled at C/3 after an extra cycle at C/10. The discharge capacity suddenly drops to 60% of the initial value, and the Coulombic efficiency becomes unstable, as shown in the inset of Fig. 4(a). After 20 cycles, the pressure control fixture was reapplied to the pouch cell with one cycle at C/10 then back to C/3. It is worth noted that the capacity recovers to 90% of the initial value, and the Coulombic efficiency is back to stable. This fixture was then kept for the subsequent 700 cycles, and the capacity retention reaches 58.7% at the end of cycling.

To analyze the degradation mechanism of the LNMO-Graphite system, the cycled pouch cell was disassembled, and both electrodes were collected and then reassembled into half cells. The cycle performances of these half cells are illustrated in Fig. 4(b), and (c). The "initial discharge capacity" for the cathode is around 100 mAh·g^{-1}, which is lower than the fresh cathode (up to 135 mAh·g^{-1}). Interestingly, the discharge capacity of the cycled cathode in the following cycles increases up to 117 mAh·g^{-1} with recovery percentage (compare with the fresh cathode) of 87.4% at the C/10 rate and 80.8% at the C/3 rate. As for the graphite anode, the recovery percentage is only 53.9%, even with the C/20 rate. These post-mortem analyses indicate that the degradation mechanism of LNMO-Graphite full cell is not solely caused by the failure of the LNMO cathode; the graphite anode degrades even more after ultra-long cycling. It has been proposed in the literature that the cross-talk between the positive and negative electrodes is extraordinarily complex and detrimental for this system. During the high voltage operation, electrolyte decomposition on the cathode side is unavoidable; an increasing amount of HF as one of the main by-products would etch the surface of the LNMO material, leading to the transition metal dissolution. These dissolved metal ions can migrate from the cathode to the anode and then reduced/deposited on the anode surface. The transition metal redeposition can act as either the poison to the graphite or the catalyst to deteriorate the interphase of the graphite anode, leading to the gradual

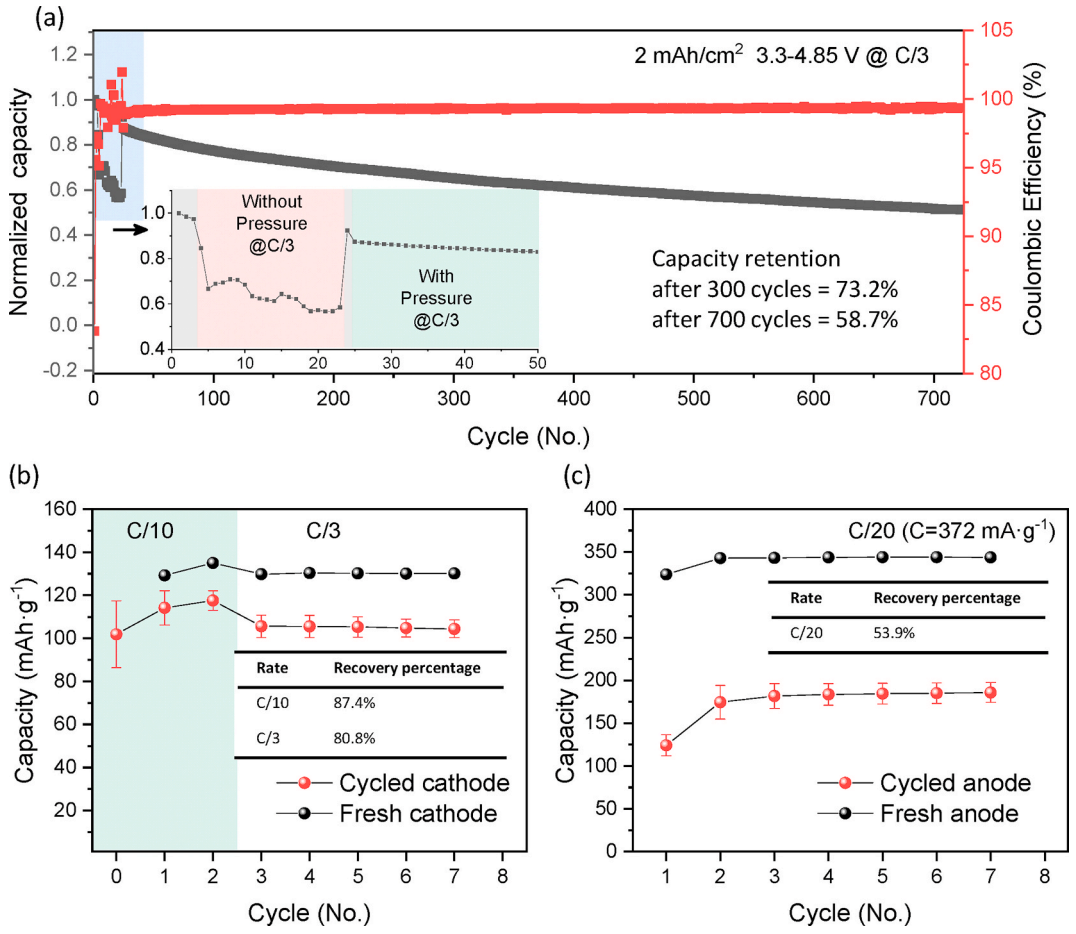

Fig. 4. (a) The stacking pressure effect on the 2 mAh·cm^{-2} pouch cell cycle performance; performance comparison between fresh and cycled (b) cathode and (c) anode (the cycled electrodes are from the single-layer pouch cell in (a)).

inactivation [16,48]. The deterioration of the interphase on the graphite side would also continually consume active lithium to form fresh interphase, which will significantly decrease the amount of active lithium inside the system [31]. Furthermore, the continuing generated gas inside can behave as the passivator to the graphite, destroying the layered structures where lithium ions intercalated into. A study is ongoing to further deconvolute degradation factors and quantify the capacity loss resulting from each factor.

Finally, a 3 mAh·cm^{-2} LNMO electrode with 3.6 mAh·cm^{-2} graphite was paired to demonstrate the long cycle stability utilizing the optimized cell components and testing conditions. More details of both electrodes can be found in Figure S4 and Table S15, including the active material, electrode thickness, porosity, and composition ratio. The cycling performance, together with Coulombic efficiency and energy efficiency, is illustrated in Fig. 5. The capacity retention is 72% after 300 cycles for the coin cell, and the Coulombic efficiency reaches 99.9% after 100 cycles. Fig. 5(b) shows the electrochemical cycling data of the pouch cell with the stacking pressure control fixture. Cycle retention 78% has been achieved after 300 cycles of the pouch cell with the thick LNMO electrode. To our best knowledge, this value of capacity retention based on the thick LNMO electrode has never been reported before. The related dQ/dV plot shown in Figure S10(a) and (b) illustrates the reason

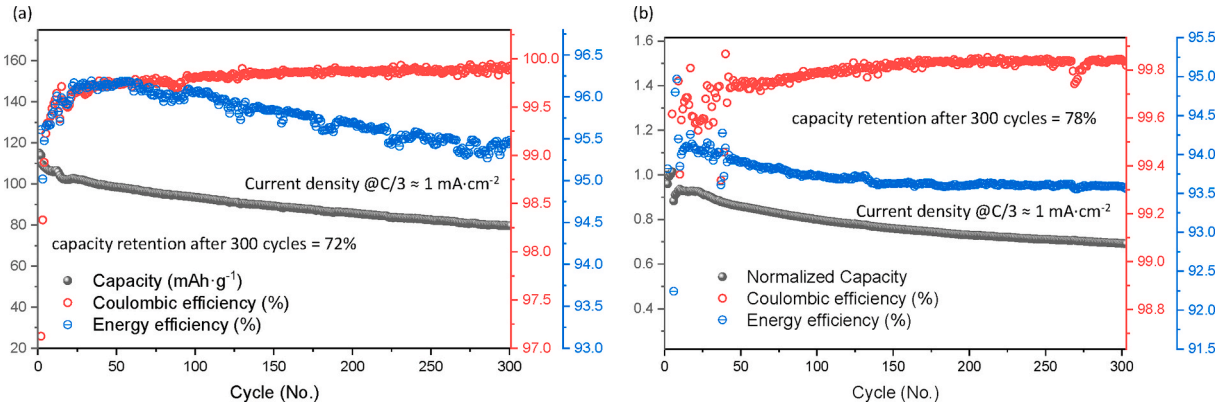

Fig. 5. Full cell cycling performance with the 3 mAh·cm^{-2} electrodes in (a) coin cell and (b) pouch cell.

for the major capacity loss in the coin cell and pouch cell, respectively. The oxidation peaks continue to move towards the right side while the reduction peaks move to the left, implying an increase of impedance inside the full cell during cycling. It is worth noting that the Coulombic efficiency takes more than tens of cycles to be stabilized, which is different from the conventional LCO/LFP/NCA-graphite cases with much lower charge cut-off voltage. The electrolyte decomposition can be the primary reason for the low Coulombic efficiency at the beginning. Other modification strategies such as novel electrolytes with additive and electrode surface coating are required to further improve the cycling stability of the thick LNMO-graphite electrode system. The rate performance of full cell with the thick LNMO electrode and graphite was also tested using a coin cell, and the results are shown in Figure S10(c). So far, the rate performance of LNMO-graphite full cell needs further engineering optimizations since the thickness here for the cathode is around 80 μm. The better distribution of conductive agent or the recently reported imbedded carbon nanotubes [49] may have a chance to improve the rate performances of full cell with LNMO thick electrode.

4. Conclusion

In summary, we have benchmarked and optimized the electrochemical performance of thick LNMO electrodes in various full cell formats. It has been found that all the components, including the binder, the conductive agent, the ratio between these two and the active materials, the cell setups, and the stacking pressure control are essential for supporting excellent long-term electrochemical performance. As a result of the optimization, 70% and 78% capacity retentions have been achieved after 300 cycles for the thick LNMO electrode (3 $mAh{\cdot}cm^{-2}$ areal capacity loading) in a coin cell and pouch cell, respectively. The post-mortem analyses illustrate that the source of the degradation for the LNMO-graphite cell is from the drastic cross-talk between the positive and negative electrodes. The LNMO cathode turns out to be more robust than the graphite anode under high voltage (up to 4.85 V) in the full cell. Further explorations on the mechanism of both electrolyte decomposition and graphite degradation with the integrated modification strategies will ultimately enable LNMO-graphite batteries in the marketplace for portable electronics, electric vehicles, and household energy storage devices.

Author contributions

W.L., M.Z., and Y.S.M. conceived the idea. W.L. performed the cathode characterization, summarized the cathode comparison. Y.C performed the pouch cell test. W.Y. and Y.L. performed the conductive agent, binder, and coin cell setup comparison. A.C. conducted the full coin cell test. R.S. collected and analyzed the ICP data. All authors discussed the results and commented on the manuscript. All authors have approved the final manuscript.

Declaration of competing interest

The authors declare no competing interests.

CRediT authorship contribution statement

Weikang Li: Writing - original draft, Conceptualization, Methodology, Investigation. **Yoon-Gyo Cho:** Methodology, Investigation. **Weiliang Yao:** Methodology, Investigation. **Yixuan Li:** Methodology, Investigation. **Ashley Cronk:** Methodology, Investigation. **Ryosuke Shimizu:** Methodology, Investigation. **Marshall A. Schroeder:** Resources, Writing - review & editing. **Yanbao Fu:** Resources, Validation. **Feng Zou:** Resources, Validation. **Vince Battaglia:** Supervision. **Arumugam Manthiram:** Supervision. **Minghao Zhang:** Writing - review & editing, Conceptualization. **Ying Shirley Meng:** Writing - review & editing, Conceptualization, Supervision.

Acknowledgment

This material is based upon the work supported by the U.S. Department of Energy's Office of Energy Efficiency and Renewable Energy (EERE) and U.S. Army Tank & Automotive Research Development and Engineering Command (TARDEC) under the award number: DE-EE0008442. XRD, and SEM were performed at the San Diego Nanotechnology Infrastructure, a member of the National Nanotechnology Coordinated Infrastructure, which is supported by the US National Science Foundation (NSF) (grant ECCS-1542148). W.L. thanks Neware Instruments for the Neware battery test system. W.L. thanks Prof. Zhaoping Liu's group from Ningbo Institute of Materials Technology & Engineering (NIMTE) for providing NM-LNMO materials and NIMTE graphite anode.

Appendix A. Supplementary data

Supplementary data to this article can be found online at https://doi.org/10.1016/j.jpowsour.2020.228579.

References

[1] L. Wang, B. Chen, J. Ma, G. Cui, L. Chen, Chem. Soc. Rev. 47 (2018) 6505–6602.
[2] M. Li, J. Lu, Z. Chen, K. Amine, Adv. Mater. (2018), e1800561.
[3] M. Gu, A. Genc, I. Belharouak, D.P. Wang, K. Amine, S. Thevuthasan, D.R. Baer, J. G. Zhang, N.D. Browning, J. Liu, C.M. Wang, Chem. Mater. 25 (2013) 2319–2326.
[4] M. Wentker, M. Greenwood, J. Leker, Energies 12 (2019).
[5] M. Li, J. Lu, Science 367 (2020) 979–980.
[6] N. Zhang, N. Zaker, H. Li, A. Liu, J. Inglis, L. Jing, J. Li, Y. Li, G.A. Botton, J. R. Dahn, Chem. Mater. 31 (2019) 10150–10160.
[7] H. Li, M. Cormier, N. Zhang, J. Inglis, J. Li, J.R. Dahn, J. Electrochem. Soc. 166 (2019) A429–A439.
[8] J. Lee, A. Urban, X. Li, D. Su, G. Hautier, G. Ceder, Science 343 (2014) 519–522.
[9] J. Lee, D.A. Kitchaev, D.H. Kwon, C.W. Lee, J.K. Papp, Y.S. Liu, Z. Lun, R. J. Clement, T. Shi, B.D. McCloskey, J. Guo, M. Balasubramanian, G. Ceder, Nature 556 (2018) 185–190.
[10] D.A. Kitchaev, Z.Y. Lun, W.D. Richards, H.W. Ji, R.J. Clement, M. Balasubramanian, D.H. Kwon, K.H. Dai, J.K. Papp, T. Lei, B.D. McCloskey, W. L. Yang, J. Lee, G. Ceder, Energy Environ. Sci. 11 (2018) 2159–2171.
[11] F. Wu, W.K. Li, L. Chen, J. Wang, W.R.G.M.L. Bao, Y. Lu, J. Tan, S. Chen, R.J. Chen, Y.F. Su, J. Power Sources 402 (2018) 499–505.
[12] S. Hy, H.D. Liu, M.H. Zhang, D.N. Qian, B.J. Hwang, Y.S. Meng, Energy Environ. Sci. 9 (2016) 1931–1954.
[13] S.H. Park, S.W. Oh, S.H. Kang, I. Belharouak, K. Amine, Y.K. Sun, Electrochim. Acta 52 (2007) 7226–7230.
[14] H.M. Wu, I. Belharouak, H. Deng, A. Abouimrane, Y.K. Sun, K. Amine, J. Electrochem. Soc. 156 (2009).
[15] J. Alvarado, M.A. Schroeder, M. Zhang, O. Borodin, E. Gobrogge, M. Olguin, M. S. Ding, M. Gobet, S. Greenbaum, Y.S. Meng, K. Xu, Mater. Today 21 (2018) 341–353.
[16] J. Ma, P. Hu, G. Cui, L. Chen, Chem. Mater. 28 (2016) 3578–3606.
[17] B. Aktekin, M.J. Lacey, T. Nordh, R. Younesi, C. Tengstedt, W. Zipprich, D. Brandell, K. Edström, J. Phys. Chem. C 122 (2018) 11234–11248.
[18] A. Kraytsberg, Y. Ein-Eli, Adv. Energy Mater. 2 (2012) 922–939.
[19] H. Xu, H. Zhang, J. Ma, G. Xu, T. Dong, J. Chen, G. Cui, ACS Energy Lett. 4 (2019) 2871–2886.
[20] Y. Kuang, C. Chen, D. Kirsch, L. Hu, Adv. Energy Mater. 9 (2019).
[21] L. Li, R.M. Erb, J. Wang, J. Wang, Y.-M. Chiang, Adv. Energy Mater. 9 (2019).
[22] C. Arbizzani, F. De Giorgio, M. Mastragostino, J. Power Sources 266 (2014) 170–174.
[23] C.K. Kim, K. Kim, K. Shin, J.J. Woo, S. Kim, S.Y. Hong, N.S. Choi, ACS Appl. Mater. Interfaces 9 (2017) 44161–44172.
[24] M.S. Milien, H. Beyer, W. Beichel, P. Klose, H.A. Gasteiger, B.L. Lucht, I. Krossing, J. Electrochem. Soc. 165 (2018) A2569–A2576.
[25] A. Hofmann, A. Höweling, N. Bohn, M. Müller, J.R. Binder, T. Hanemann, Chemelectrochem 6 (2019) 5255–5263.
[26] B. Michalak, B.B. Berkes, H. Sommer, T. Brezesinski, J. Janek, J. Phys. Chem. C 121 (2016) 211–216.
[27] Y. Li, G.M. Veith, K.L. Browning, J. Chen, D.K. Hensley, M.P. Paranthaman, S. Dai, X.-G. Sun, Nano Energy 40 (2017) 9–19.
[28] M. Mancini, P. Axmann, G. Gabrielli, M. Kinyanjui, U. Kaiser, M. Wohlfahrt-Mehrens, ChemSusChem 9 (2016) 1843–1849.
[29] S. Solchenbach, M. Wetjen, D. Pritzl, K.U. Schwenke, H.A. Gasteiger, J. Electrochem. Soc. 165 (2018) A512–A524.
[30] F. De Giorgio, N. Laszczynski, J. von Zamory, M. Mastragostino, C. Arbizzani, S. Passerini, ChemSusChem 10 (2017) 379–386.
[31] A. Höweling, S. Glatthaar, D. Nötzel, J.R. Binder, J. Power Sources 274 (2015) 1267–1275.

[32] J.-H. Kim, N.P.W. Pieczonka, P. Lu, Z. Liu, R. Qiao, W. Yang, M.M. Tessema, Y.-K. Sun, B.R. Powell, Adv. Mater. Interfaces 2 (2015).
[33] T.J. Lee, J.B. Lee, T. Yoon, D. Kim, O.B. Chae, J. Jung, J. Soon, J.H. Ryu, J.J. Kim, S.M. Oh, J. Electrochem. Soc. 163 (2016) A898–A903.
[34] L. Hu, K. Amine, Z. Zhang, Electrochem. Commun. 44 (2014) 34–37.
[35] Y.-M. Song, J.-G. Han, S. Park, K.T. Lee, N.-S. Choi, J. Mater. Chem. 2 (2014) 9506–9513.
[36] B.H. Toby, R.B. Von Dreele, J. Appl. Crystallogr. 46 (2013) 544–549.
[37] H. Deng, I. Belharouak, Y.K. Sun, K. Amine, J. Mater. Chem. 19 (2009) 4510–4516.
[38] A. Kajiyama, R. Masaki, T. Wakiyama, K. Matsumoto, A. Yoda, T. Inada, H. Yokota, R. Kanno, J. Electrochem. Soc. 162 (2015) A1516–A1522.
[39] T. Yoon, S. Park, J. Mun, J.H. Ryu, W. Choi, Y.-S. Kang, J.-H. Park, S.M. Oh, J. Power Sources 215 (2012) 312–316.
[40] Y. Tang, J. Deng, W. Li, O.I. Malyi, Y. Zhang, X. Zhou, S. Pan, J. Wei, Y. Cai, Z. Chen, X. Chen, Adv. Mater. 29 (2017).
[41] X. Chen, W. Xu, J. Xiao, M.H. Engelhard, F. Ding, D. Mei, D. Hu, J. Zhang, J.-G. Zhang, J. Power Sources 213 (2012) 160–168.
[42] F. Wu, W.K. Li, L. Chen, Y. Lu, Y.F. Su, W. Bao, J. Wang, S. Chen, L.Y. Bao, J. Power Sources 359 (2017) 226–233.
[43] S. Zhang, H. Gu, H. Pan, S. Yang, W. Du, X. Li, M. Gao, Y. Liu, M. Zhu, L. Ouyang, D. Jian, F. Pan, Adv. Energy Mater. 7 (2016).
[44] C. Zhan, Z.P. Yao, J. Lu, L. Ma, V.A. Maroni, L. Li, E. Lee, E.E. Alp, T.P. Wu, J. G. Wen, Y. Ren, C. Johnson, M.M. Thackeray, M.K.Y. Chan, C. Wolverton, K. Amine, Nat. Energy 2 (2017) 963–971.
[45] I. Belharouak, G.M. Koenig, J. Ma, D.P. Wang, K. Amine, Electrochem. Commun. 13 (2011) 232–236.
[46] J. Xiao, Science 366 (2019) 426–427.
[47] B. Michalak, B.B. Berkes, H. Sommer, T. Bergfeldt, T. Brezesinski, J. Janek, Anal. Chem. 88 (2016) 2877–2883.
[48] J.-H. Kim, N.P.W. Pieczonka, Z. Li, Y. Wu, S. Harris, B.R. Powell, Electrochim. Acta 90 (2013) 556–562.
[49] J. Hu, B. Wu, X. Cao, Y. Bi, S. Chae, C. Niu, B. Xiao, J. Tao, J. Zhang, J. Xiao, J. Power Sources (2020) 454.